Cellular and Molecular Biology

Journal homepage: www.cellmolbiol.org

Preparation of BSA-coated Au Nanoparticles Contrast Agent and Its Application in PETCT Imaging

Jing Wei[1*], Pingwei Li[2], Huai Zhang[1], Ronghua Zhu[1]

[1]*Department of Nuclear Medicine, Huai'an First People's Hospital, Huai'an, 223300, Jiangsu Province, China*

[2]*Department of Radiotherapy, Huai'an First People's Hospital, Huai'an, 223300, Jiangsu Province, China*

ARTICLE INFO

Review paper

Article history:
Received: November 15, 2021
Accepted: March 07, 2022
Published: March 31, 2022

Keywords:
Bovine Serum Albumin, Gold Nanoparticles, Contrast Agent Preparation, PET/CT Imaging

ABSTRACT

Tumors are the biggest opponents in the history of human diseases, and they cannot be eliminated so far. The only way to treat tumors is to detect them early so that the survival rate can be improved by early treatment. For tumor detection, CT scan is the most commonly used, and PET/CT is an enhanced version of CT technology. Although PET/CT can produce relatively clear images of the human body, due to the complex structure of the human body, there are many ghosts and shadows, and the images cannot be accurately judged. Therefore, this paper aims to prepare high-definition nanoparticle contrast agents, hoping to make PET/CT images clearer and easier to distinguish. In this paper, the advantages of gold nanoparticles are fully analyzed for the preparation of contrast agents, and a gold nano-contrast agent coated with bovine serum albumin (BSA) is proposed. Gold nanoparticles (GNRs) were prepared by the traditional induction method and their properties were analyzed. Finally, taking mice as the experimental object, a comparative experiment was carried out, and the toxicological and optical properties were analyzed. The experimental results show that the adsorption performance of the BSA-coated gold nanoparticles prepared in this paper is more than 90% at different temperatures. And through the comparison experiment, the contrast agent prepared in this paper has an increased signal-to-noise(StN) ratio change rate of more than 50%, which can be well applied to PET/CT imaging.

DOI: http://dx.doi.org/10.14715/cmb/2022.68.3.19

Introduction

PET/CT is a new type of anatomical imaging tracer equipment with two main imaging tracer techniques: PET (human functional metabolic cell forming body) and CT (human positron structure description). The imaging tracer process is mainly to inject a small amount of tracer into a human body first, and after a period of time, the tracer is completely and evenly distributed and injected into the human body (1). The post-processing of PET/CT combines the information of anatomy and human functional metabolites, which makes it have high morphological sensitivity, specificity and high accuracy for the early localization diagnosis and staging treatment of central tumor lung cancer. The value of CT and PET in the early diagnosis and treatment of central lung cancer is mainly reflected in the ability to clearly and accurately display the histomorphological and pathological characteristics of human tumors and to observe the various histological characteristics of human tumors. Post-processing can also help to accurately display the tumor and surrounding tissues of the human body, which has a great influence and help in the early localization, diagnosis, staging, prognosis and treatment of lung cancer. However, the current PET/CT contrast agents have more or fewer defects, so it is necessary to study PET/CT contrast agents now (2,3).

First, a series of preprocessing is performed on the PET/CT images. The preprocessing operations used here include interpolation and denoising PET/CT registration. Because the various brands of the current PET/CT all-in-one machine are different, the generated image standards are also slightly different. Even the same sequence of images of the same machine requires further registration work to meet the needs of doctors for diagnosis and image processing. This paper proposes a rigid registration algorithm based on a human silhouette to solve the registration problem. Secondly, a BSA-coated gold nanoparticle contrast agent was designed and prepared.

With the further development of three-dimensional

*Corresponding author. E-mail: qitanyun99030629@163.com

image conformal and conformal image intensity modulation techniques in radiotherapy imaging technology and the extensive research and application in clinical radiotherapy. In tumor radiotherapy, more and more attention has been paid to the precise location of the target area and the delineation of the image, especially the development of the PET/CT image integrated machine in 2000 and the clinical application of radiotherapy. Karim N's research found that F18-FDG PET/CT is a valuable imaging method. It is used to show active foci of glucose metabolism in lung parenchymal lesions, preoperative assessment and as a baseline scan for patient monitoring (1). The study by Sadaghiani M S discussed the possible application of artificial intelligence in 18F-FDG PET imaging (2). Saer studied the diagnosis of inflammation of the aorta in GCA by PET/CT(3). Dhull RS focused on the technique, interpretation, indications, and recent practice guidelines of renal scintigraphy in children with nephropathy (4). Hu C's study explored the value of fusion pretreatment functional imaging (18F-FDG PET/CT) radiomics for modeling local recurrence in head and neck cancer. His experiments demonstrated that radiomics models based on PETCT fusion were superior to PET- or CT-based models alone in predicting local recurrence, and the inclusion of clinical parameters may lead to more accurate predictions, which are important for the development of personalized and precise treatment regimens (5). Although PET/CT is also more convenient in image processing, radiotherapy PET and CT are organically and closely integrated. It has the common advantages and advantages of the two image devices, and the patient completely avoids the tedious operation steps of multiple image scans, which is conducive to the accurate scanning and positioning of the target area of the lesion. It guides the precise setting and positioning of the high-dose target area of radiotherapy, which helps to further increase the dose of the target area of tumor lesions and effectively reduce the dose of normal tumor tissue irradiation. However, due to the inherent shortcomings of the technology, more efficient contrast agents must be used to improve the contrast and clarity of the images.

Many scholars have put forward different opinions on the research of contrast agents, but there is a similarity, that is, the application of precious metal nanoparticles. Baek S found that nanoparticle agents combined with targeting factors that respond to lesions enable specific CT imaging. Therefore, he proposed a new data-driven approach for the identification of nanoparticulate agents using PCD (6). Zhao W studied biocompatible bovine serum albumin (BSA)-coated gold nanoparticles (Au NPs) (7). Kee PH has developed a potentially clinically useful X-ray molecular imaging contrast agent based on gold nanoparticles (AuNPs). It is functionalized with collagen-binding adhesion protein 35 (CNA35), capable of prolonging blood pool enhancement for coronary angiography and specifically targeting collagen within myocardial scars (8). After the description of relevant research, we can clearly find that the shortcomings of the current PET/CT technology still have the defects of contrast agents. Reagents with clear contrast are often toxic, and non-toxic contrast is not clear enough. Therefore, the gold nanomaterials coated with BSA can solve this problem.

BSA-Coated Gold Nanomaterials and PEC/CT Imaging

PETCT Imaging

The PET/CT diagnostic device is a new type of positron-electron medical imaging diagnostic equipment that integrates positron emission mechanical tomography PET and CT mechanical tomography. Its success has caused a strong shock to the medical community and researchers and brought hope to the lives of millions of patients with advanced cancer. Compared with separate PET anatomical images and CT images, the PET/CT robot not only greatly reduces the image scanning time, but also effectively reduces the various high-dose ultraviolet radiation that patients receive during image shooting. PET/CT also fundamentally and effectively solves the problems and drawbacks of unclear images in traditional nuclear medicine anatomical images during structural scanning. And technically, the CT structural image information is combined with comprehensive correction, so that the nuclear medicine anatomical structure image can truly achieve the purpose of quantitative structural scanning. It realizes the complementary combination of traditional PET and CT structural image information and gives full play to their respective technical advantages (9-10).

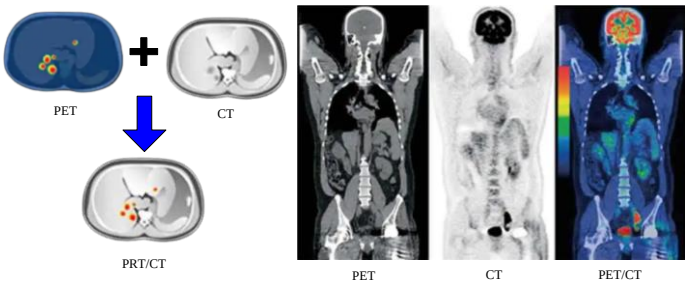

Figure 1. PET/CT image

As shown in Figure 1: There are indeed many essential connections and differences between PET images and other CT images. The image provided by CT is an image showing the rich anatomical structure of human tissue parts. In clinical practice, it is generally by changing the window width and window level of the human body structure image to help patients obtain rich anatomical organization maps of different human anatomical tissue structures. The size of the image is large and the definition is relatively high. In general, the edge of the tumor lesion is better determined. PET/CT images have a profound impact and significance on the early medical diagnosis and early identification, diagnosis and treatment of tumor patients. For some patients with poor prognoses, tumor discovery and treatment have certain predictive and control effects. Cancer patients, can have a real-time understanding of their tumor disease and its development, and cooperate with oncologists to further treat them. For oncologists, they can take appropriate tumor treatment measures and means according to their real-time conditions, and control the appropriate amount of drugs and doses. Inappropriate medication can be avoided, causing unnecessary psychological damage to the patient's body or unintended consequences on the efficacy of the drug.

Interaction of BSA with Gold Nanoparticles

Gold nanoparticles (GNPs) have numerous specific advantages, as shown in Figure 2. First, GNPs are relatively simple to synthesize and have high stability. Secondly, GNPs have a high specific surface area and are easy to lap with ligands to obtain good biocompatibility, which provides a guarantee for their biological applications. Furthermore, the unique optoelectronic properties of GNPs can be controllably regulated by means of size, shape, and chemical modification. Finally, GNPs provide a platform for the modification of bio-multifunctional ligands and the combination of small molecules (11).

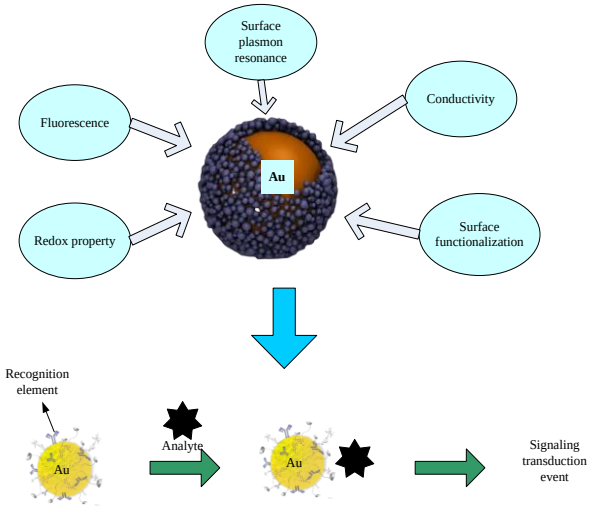

Figure 2. Schematic diagram of physical properties and detection system of GNPs-based materials

The quantum size effect of GNPs enables them to have discontinuous electronic transition energy levels, which brings them many electronic and optoelectronic properties such as molecular-like redox reactions, quantized capacitive charging, and surface plasmon resonance (SPR) effects (12-13). Since the SPR bands of GNPs are in the visible region, GNPs are darker at room temperature. In addition, factors such as size, shape, ligand, temperature, solvent, and particle spacing can have an important impact on the SPR effect of particles (14-15). It is worth noting that the SPR frequency is very sensitive to the aggregation state of the nanoparticles. Due to the effect of inter-particle plasmon coupling, particle agglomeration will cause its spectral red shift, which in turn causes the color of its solution to change from red to blue, which is beneficial for GNPs to be used in colorimetric sensors (16-17). GNPs can be used for a variety of biosensing targeting agents, mainly due to their unique physicochemical properties, including quantum size effect, SPR, SERS, and FoDrster resonance energy transfer (FRET). For example, using the FRET effect of GNPs can complete the efficient detection of various targets such as DNA, mRNA and protein.

PET/CT Image Segmentation Algorithm

There are many commonly used image segmentation algorithms, and it is also very common

to apply to medical images. Most of the methods have the disadvantage of not being universally applicable because of the blurred boundary of the tumor target area and an obvious transition area in PET images. This leads to the need to set different algorithm parameters for the PET images of different central lung cancer patients to achieve accurate segmentation of the tumor target area of the current PET image.

(i) Traditional edge detection operator

The Roberts operator is relatively simple in many commonly used operators for edge image detection. It often needs to be more refined for the approximate edge gradient magnitude image detected by the above Roberts operator, and the efficiency and accuracy of edge gradient magnitude location are not very high. The definition formula of edge gradient magnitude is:

$$g(x,y)=\sqrt{[f(x,y)-f(x+1,y+1)]^2+[f(x,y+1)-f(x+1,y)]^2} \quad [1]$$

$$M(x,y)=mag(\nabla f) \quad [2]$$

Therefore, the convolution template of the gradient can be calculated in the form of a 2×2 convolution kernel.

The Sobel difference operator calculates the partial derivative difference function in the x and y directions on a 3×3 neighborhood with the f(x,y) neighborhood as the center of the image. The formula is defined as follows:

$$S_x=\{f(x+1,y-1)+2f(x+1,y)\}-\{f(x-1,y-1)+2f(x-1,y+1)\} \quad [3]$$
$$S_y=\{f(x-1,y+1)+2f(x,y+1)\}-\{f(x-1,y-1)+2f(x,y-1)\} \quad [4]$$

So the magnitude of the calculated gradient is:

$$g(x,y)=\sqrt{(S_x)^2+(S_y)^2} \quad [5]$$

A second-order differential linear operator is directly selected instead of a first-order differential linear operator. Its expression is:

$$\nabla^2 f(x,y)=\frac{\partial^2 f(x,y)}{\partial x^2}+\frac{\partial^2 f(x,y)}{\partial y^2} \quad [6]$$

To be more suitable for digital image processing, the formula is expressed in discrete form:

$$\nabla^2 f(x,y)=f(x+1)+f(x-1,y)+f(x,y+1)+f(x,y-1)-4f(x,y) \quad [7]$$

Canny multi-level system edge performance detection method operator criterion is an electronic algorithm for multi-level system edge performance detection. It is an operator for edge performance detection of multi-level systems based on the latest canny electronic algorithm, which is newly proposed based on the latest optimized edge performance detection electronic algorithm. And this paper mainly gives a kind of three multi-level edge performance detection operator criteria for analyzing and evaluating the comprehensive performance of various algorithms and their pros and cons. The design and implementation of the Canny operator and the specific steps of the process are described as follows:

To smooth the image, in order to reduce the influence of noise on the gradient calculation, the operator uses the first derivative of the two-dimensional Gaussian function to blur the image. The two-dimensional Gaussian function is:

$$G(x,y)=\frac{1}{2\pi\sigma^2}sxp\left(-\frac{x^2+y^2}{2\pi\sigma^2}\right) \quad [8]$$

Among them, the size of σ can control the degree of smoothing of the image.

In order to calculate the gradient magnitude and direction of the image, the Canny operator calculates the gradient magnitude components in the vertical and horizontal directions using the first-order difference in the 2 × 2 field. The gradient components obtained in the x-direction and the y-direction are $f_x(x,y)$ and $f_y(x,y)$ respectively, and the calculation formula is as follows:

$$f_x(x,y)=[f(x+1,y)-f(x,y)+f(x+1,y+1)-f(x,y+1)]/2 \quad [9]$$
$$f_y(x,y)=[f(x,y+1)-f(x,y)+f(x+1,y+1)-f(x+1,y)]/2 \quad [10]$$

So, the gradient magnitude of the point (x,y) is:

$$M(x,y)=|\nabla f(x,y)|=\sqrt{f_x^2(x,y)+f_y^2(x,y)} \quad [11]$$

It can also be simplified to:

$$M(x,y)=|f_x(x,y)|+|f_y(x,y)| \quad [12]$$

The gradient direction angle at point (x,y) is:

$$\theta(x,y)=\arctan\left(\frac{f_y(x,y)}{f_x(x,y)}\right) \quad [13]$$

(ii) Otsu algorithm

The Otsu Binary Algorithm (OTSU) is a mathematical algorithm used to calculate the inter-class threshold for binary segmentation of grayscale images. The binary segmentation method is also sometimes referred to as the maximum between-class

variance segmentation method. It is based on the binary segmentation principle of the Otsu method to traverse the grayscale and background of the image to obtain the best segmentation threshold. After the background of the grayscale image is binarized, the variance between the two classes of the image's foreground and the image background is the largest. Because its binary segmentation principle is simple, and the uniformity is not directly affected by the brightness and color contrast of the image, it has been widely used in the grayscale processing of images (18-19). For image I(x,y), the segmentation threshold between the foreground (target region of interest) and the background is denoted as T, ω1 is the ratio of the foreground pixels to the whole image pixels, and μ1 represents its average gray level. ω2 is the ratio of the number of background pixels to the pixels of the whole image.

$$\omega 1=\frac{N1}{M\times N} \quad [14]$$

$$\omega 2=\frac{N2}{M\times N} \quad [15]$$

$$N1+N2=M\times N \quad [16]$$

$$\mu=\mu 1\times\omega 1+\mu 2\times\omega 2 \quad [17]$$

$$g=\omega 1\times[\mu-\mu 1)+\omega 2\times(\mu-\mu 2) \quad [18]$$

$$g=\omega 1\times\omega 2\times(\mu-\mu 2)^2 \quad [19]$$

The threshold T that maximizes the variance between classes is obtained by traversing each gray level of the image, which is the desired value.

(iii) Algorithm analysis

The above four operators similar to traditional methods for edge detection perform edge detection on the data of the PET/CT original detection image. The threshold selection of the edge detection operator used in this paper is the best threshold selected automatically. The threshold parameters of each operator are shown in Table 1. As can be seen from the table, when the traditional edge detection operator is used on the original image, the threshold difference of each patient image is not particularly large.

Table 1. Threshold parameters of traditional edge detection operators for PET raw image detection

	Rv	Sv	Lv	Cv1	Cv2
patient A	1.05e+3	1.07e+3	17.54	0.0063	0.0151
patient B	976.5	999.6	11.74	0.0065	0.0156
patient C	783.1	761.7	15.38	0.0063	0.0156
patient D	880.7	878.1	14.64	0.0063	0.0156
patient E	1.15e+3	1.1e+3	16.92	0.0063	0.0156

In Table 1, Rv represents the threshold parameter of the Roberts operator, Sv represents the threshold parameter of the Sobel operator, Lv represents the threshold parameter of the Laplace operator, and Cv1 and Cv2 represent the dual-threshold parameters of the Canny operator.

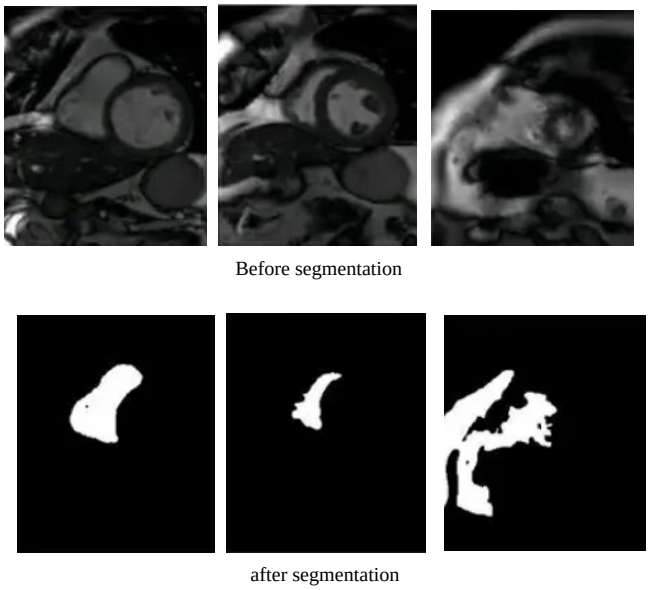

Figure 3. Otsu algorithm segmentation

Since the Otsu algorithm is an adaptive threshold determination algorithm, manual parameter adjustment is not required. When the algorithm is applied to the data image, although it can have a good effect on the segmentation of a part of the image data, it cannot be applied to all the image data. The most obvious is the phenomenon of over-segmentation. As shown in Figure 3, the segmentation effect of the previous case is very good, but the segmentation of the next image is over-segmented. In some cases, over-segmentation is more serious. There are two reasons. One is the SUV value image used. The SUV value of each patient may be different, which leads to the general method not having universal applicability. The other is that the Otsu algorithm is based on the threshold segmentation with the largest inter-class variance, and there is usually a transition area around the tumor lesion area in the PET image. When the calculated threshold has slight fluctuations, it will cause obvious over-segmentation or under-segmentation.

Preparation of BSA-Coated Gold Nanoparticles Contrast Agent

Overview and Preparation of BSA-GNPs

For larger magnetic materials, the composition, crystal structure and magnetic anisotropy of the material will affect its properties, such as coercivity and magnetic susceptibility. However, when the size of magnetic materials is reduced to nanometers, the effect of size on magnetism becomes particularly important, and a unique phenomenon, superparamagnetism, arises from the size dependence of JVTNTPS. For magnetic materials, the magnetic anisotropy energy barrier from the upper spin state to the lower spin state is proportional to the magnetic anisotropy constant (K_u) and the volume (V). For large-sized magnetic materials, the magnetic anisotropy energy (K_T) is much larger than the thermal energy, so only the thermal energy cannot overcome the magnetic anisotropy energy. However, for smaller nanoparticles, although the thermal energy is not enough to overcome the spin-spin exchange coupling energy, it is sufficient to reverse the magnetic spin direction. Such magnetic fluctuations result in zero remanences under an applied circulating magnetic field, a phenomenon known as superparamagnetism. For magnetic materials with a fixed size, the superparamagnetic phenomenon can also be produced by changing the temperature. The temperature at which the magnetic material changes from paramagnetic to superparamagnetic is called the critical transition temperature (K_b).

Experimental Drugs and Instruments

The drug and device information used in this chapter are listed in Tables 2 and 3, respectively.

Preparation Process

GNRs were made utilizing the traditional seed induction process, with a few modest tweaks based on past research. In a 25 mL Erlenmeyer flask, 4.5 mL ultrapure water, 5 mL 0.2 M CTAB solution, and 1 mL 2.5 mM HAuC14 solution were slowly swirled. After that, 0.5 mL of 0.012M fresh ice-bath NaBH4 solution was added, and the solution was rapidly agitated to alter the hue from pale yellow to dark tan. The gold seed particles were held at a constant temperature of 27°C until usage after 100 seconds of continuous vigorous stirring.

Table 2. Experimental Apparatus

Instrument/equipment name	Specifications/ Models	Manufacturer
Electronic balance	JA5003	Sartorius, Germany
CNC ultrasonic cleaner	KQ-3200B	Gongyi Yuhua Instrument Co., Ltd.
Thermostatic Magnetic Stirrer	85-2	Zhengzhou Ouka Instrument Equipment Co., Ltd.
Digital display intelligent temperature control magnetic stirrer	SZCL-2A	Gongyi Zihua Instrument Co., Ltd.
refrigerator	BCD- 190HK	Henan Xinfei Electric Co., Ltd.
UV-Vis Absorption Spectrometer	TU-1810	Beijing Puxi General Equipment Co., Ltd.
transmission electron microscope	JEM 2100	Japan Electronics (JEOL) Corporation
Laser particle size analyzer	Zetasizer-NanoZS	Malven UK

Table 3. Experimental Reagents

Reagent name	Abbreviation	Manufacturer
Concentrated nitric acid	HNO3	Sinopharm Group Chemical Reagent Co., Ltd.
Concentrated hydrochloric acid	HCI	Luoyang Haohua Chemical Reagent Co., Ltd.
Chlorauric acid	HAuCl43H2O	Alfa-Aesar
Trisodium citrate	NasC6HsO7 2H2O	Alfa-Aesar
cysteine	C3H-NO2S	Sinopharm Group Chemical Reagent Co., Ltd.
glutathione	CioH17N;O6S	Sinopharm Group Chemical Reagent Co., Ltd.
mercapto polyethylene glycol	SH-PEG (2K)	Shanghai Yanyi Biological Co., Ltd.
mercapto polyethylene glycol	SH-PEG (5K)	Shanghai Yanyi Biological Co., Ltd.
mercapto polyethylene glycol carboxyl	SH-PEG-COOH (5K)	Shanghai Yanyi Biological Co., Ltd.

Characterization

The specific method is as follows: use 40 g of NaHCO3 aqueous solution to prepare glycine solutions of different concentrations (0.1-1.2 mmolL^{-1}). Subsequently, 2 mL of glycine solutions of different concentrations were mixed with 2 mL of 0.1% w/vTNBS solution and reacted at 40 °C for 120 min. Subsequently, 3 mL of HCl in ethanol (0.5 mol L^{-1}) was added to the solution to acidify for 20 min. Finally, take 1.5mL of the acidified solution, dilute it with 1.5mL of HCl in ethanol solution (0.5molL^{-1}), and measure the absorbance at 340nm wavelength with a UV-Vis spectrophotometer. A standard curve was drawn using the relationship between absorbance and glycine concentration. From the results, it can be found that in the concentration range of 0.1-1.2 mgmL^{-1}, there is a good linear relationship between the absorbance and the concentration of glycine, and the fitting degree is 0.999. From the slope of the

straight line, the extinction coefficient is 1.0452gmL-1cm^{-1}.

The TEM samples were observed on a transmission electron microscope operating at 80 kV. The preparation steps of the TEM samples are as follows: take a drop of the dispersion to be tested, dilute it with 2 mL of water, take a drop of the diluted sample and place it on a 400-mesh carbon-supported copper mesh, and dry it at 40 °C. The particle size and particle size distribution of the samples were estimated by counting at least 200 nanoparticles.

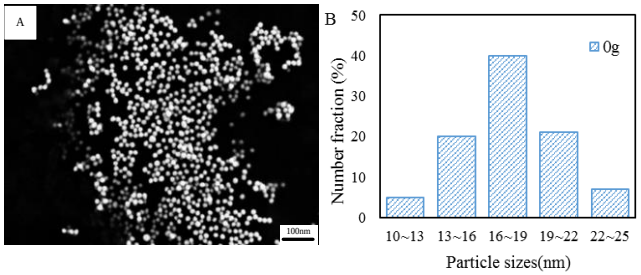

Figure 4. Preparation of gold nanoparticles

In this paper, BSA-GNPs were synthesized for the first time by co-precipitation method using OCMC as a colloidal stabilizer. Figure 4A is a TEM image of BSA-GNPs prepared by the co-precipitation method. It can be seen from the figure that the BSA-GNPs are spherical and relatively uniform in shape. According to the TEM image, the particle size and particle size distribution were calculated. The results are shown in Figure 4B. The particle size of BSA-GNPs is 18.53±2.9 nm, and the particle size is relatively uniform. However, due to the large specific surface energy of BSA-GNPs, it is easy to agglomerate, resulting in instability.

Fourier Transform Infrared Spectroscopy (FTIR)

Take a small amount of sample powder to be tested and mix with KBr powder, grind and press into tablets. Under the condition of evacuation, the infrared spectrum of the sample was measured by Fourier transform infrared spectrometer.

Figure 5A shows the infrared spectra of BSA-GNPs, OCMC and OCMC-GNPs. Two peaks appear at 577 and 3415 in the infrared spectrum of BSA-GNPs (curve a), which are the stretching vibrations of Au-O and O-H bonds, respectively. The infrared spectrum of OCMC (curve b) shows a characteristic absorption peak in the carboxyl group at 1764 and a bending vibration peak at 1597 corresponding to the N-H in the primary amine (20).

Figure 5B shows the XRD patterns of OCMC, unmodified BSA-GNPs and OCMC-GNPs, which are used to characterize the difference in their microcrystalline structures. In the XRD characterization of OCMC (curve a), only a broad diffraction peak at 22° was found, indicating that OCMC has an amorphous structure. Curve b is the XRD pattern of unmodified BSA-GNPs, it can be seen that there are six well-defined diffraction peaks at 30.1°, 35.5°, 43.3°, 53.3°, 57.3° and 63.1°, which belong to the reflective surfaces (21-22) of (220), (311), (400), (422), (511) and (440), respectively. This indicated that BSA-GNPs were successfully synthesized. These diffraction peaks can also be found in curve c, the XRD curve of OCMC-Au. From the overall analysis, it can be seen that all characteristic peaks of OCMC and unmodified BSA-GNPs appear in the XRD patterns of OCMC-GNPs, which again proves that OCMC is successfully grafted to the surface of BSA-GNPs.

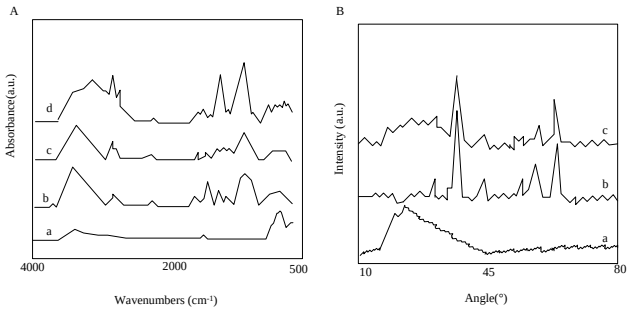

Figure 5. Infrared spectrum

Adsorption and Desorption of BSA by Gold Nanoparticles

(i) Influence of temperature on adsorption performance

Understanding the adsorption behavior of proteins is crucial for optimizing the separation performance of BSA-GNPs. Using BSA as a model protein, the effect of temperature on the adsorption behavior of BSA-GNPs on BSA was investigated, and the results are shown in Figures 6A and B. In general, the adsorption capacity of BSA-GNPs to BSA gradually increased with time, reaching equilibrium within 70 min at 25–42 °C (Figure 6A). With the increase in temperature, the equilibrium adsorption capacity of BSA first

increased and then decreased to some extent (Figure 6B). The pH of the adsorption experiment was 6.22, and under this condition, both BSA-GNPs and BSA were negatively charged. Therefore, the absorption mechanism of BSA by BSA-GNPs is mainly hydrogen bonding. Therefore, when the temperature is increased to 37~42℃, the decrease of equilibrium adsorption capacity is caused by the damage of some hydrogen bonds.

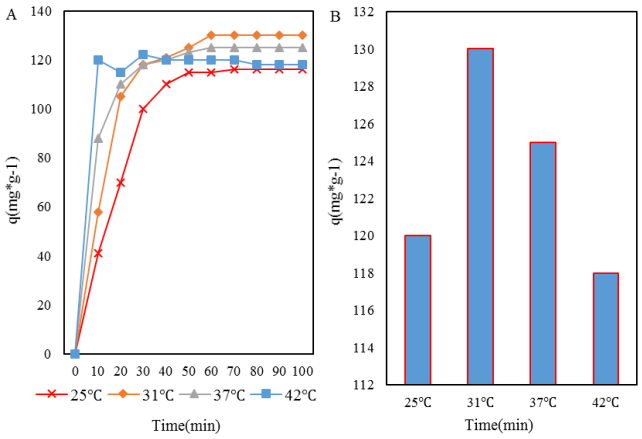

Figure 6. Effect of temperature on adsorption performance

(ii) Adsorption kinetics

The kinetics of the adsorption curves at different temperatures were simulated, with the time as the abscissa and the corresponding adsorption amounts at different temperatures as the ordinate, and the kinetics curves were drawn and simulated. The pseudo-second-order kinetic formulas used are as follows:

Quasi-Second-Order Kinetic Formulas:

$$\frac{t}{q_t}=\frac{1}{k_2 q_m^2}+\frac{t}{q_m} \quad [20]$$

Among them, k_2 is the rate constant (min-1) of the pseudo-second-order kinetic adsorption. q_m is the maximum adsorption capacity of pseudo-second-order kinetics (mg*g-1); q_t is the adsorption capacity of BSA at t (min) time (mg*g-1).

The adsorption process at different temperatures was fitted by the pseudo-second-order kinetic formula. The results are shown in Table 4 and Figure 7. As shown in Figure 7, the kinetic process of the adsorption process at different temperatures was fitted by the pseudo-second-order kinetic formula, and the equilibrium adsorption capacity q, reaction rate constant k and correlation coefficient R were obtained. It can be seen that when the temperature rises from 25°C to 42°C, the R values are all above 0.99. It shows that the adsorption kinetics of BSA on BSA-GNPs can be well described by the pseudo-second-order kinetic formula. At the same time, we found that the higher the temperature, the greater the constant of the pseudo-second-order kinetic model, indicating that the higher the temperature, the greater the adsorption rate.

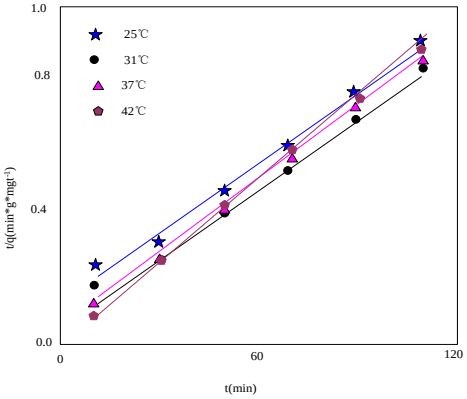

Figure 7. Pseudo-second-order kinetic linear model at different temperatures

Table 4. Kinetic parameters and correlation coefficients were calculated using the pseudo-second-order kinetic model at different temperatures

temperature	T (K)	k_2	q_m	R^2_2
25°C	298.15	3.570	144.5	0.991
31°C	304.15	6.530	150.150	0.995
37°C	310.15	18.130	132.228	0.999
42°C	315.15	22.324	122.399	0.999

Imaging Effect of BSA-Coated Gold Nanoparticles Contrast Agent

Toxicological Characteristics of BSA-Coated Gold Nanoparticles

(i) Effects on the viability of macrosomia cells in mouse peritoneal cavity

Grouping and plating: Take 3 96-well plates, and set a blank control group for each 96-well plate (without adding cell suspension, add 100 μm medium). Negative control group (adding cell suspension and adding 100 μm medium) and GAGs-GNPs group (Add UFH-GNPs and HCS-GNPs to the first 96-well plate, add LCS-GNPs and HHA-GNPs to the second 96-well plate, add LHA-GNPs to the third 96-well plate), each group was set with 5 parallel wells. The density of mouse peritoneal macrophages was adjusted to /mL with 10% FBS-DMEM cell culture medium and inoculated into the corresponding

wells of the negative control group and GAGs-GNPs group, and 100 uL of cell suspension was added to each well. 100uL of PBS was added to each well of the outer ring of the 96-well plate for sealing.

Cell culture: incubate in a CO2 cell incubator for 4h until cells adhere. After 4 h, the culture plate was shaken gently, the supernatant of each well in the culture plate was cleaned, the nonadherent cells were washed away with DMEM medium incubated at 37°C, and 10% FBS-DMEM was added to continue to incubate the cells for 24 h.

Cell drug delivery: The experimental group was given corresponding drugs (UFH-GNPs, HCS-GNPs, LCS-GNPs, HHA-GNPs, LHA-GNPs), and the concentration of iron ions was used as the standard, and the drug concentrations were set at 3.125, 6.25, 12.5, 25, and 50ug/ mL (Diluted each GAGs-GNPs in serum-free DMEM medium). Add 100uL of the drug to each well, and add 100uL of serum-free DMEM medium to each well of the blank control group and negative control group. After dosing, the 96-well plate was placed in a CO2 constant temperature incubator for 24 hours, then CCK8 was added to each well for 2 hours, and the absorbance value (OD value) of each well was detected at 450 nm.

Conclusion: The experimental results show that when the iron ion concentration is between 3.12 and 50 (ug/mL, UFH-GNPs, HHA-GNPs, LHA-GNPs, LCS-GNPs and HCS-GNPs will not have toxic effects on mouse macrophages. In contrast, GAGs-GNPs were also shown to promote the survival of mouse macrophages. Under the experimental conditions, when the iron ion concentration was 50ug/mL, GAGs-GNPs showed the greatest ability to improve the survival rate of mouse peritoneal macrophages. Their maximum survival rates were 127%, 119%, 791%, 285%, and 259%, respectively.

(ii) Detection of the influence on the coagulation system of mice

Grouping: 20 healthy adult male Kunming mice of about 20 g were randomly divided into 4 groups, with 5 mice in each group. They were divided into experimental group 1, experimental group 2, negative control group and positive control group.

Reagent: Preparation of 0.5mg/mL heparin sodium solution. Weigh 10 mg of heparin sodium (the selected heparin sodium titer is 200 U/mg), dissolve it in 2 mL of normal saline, and dilute it 10 times with normal saline to obtain a heparin sodium solution with a mass concentration of 0.5 mg/mL.

Mice tail vein administration: In the negative control group, 0.2 mL of normal saline was injected into the tail vein of each mouse. Each mouse in the positive control group was injected with 0.2 mL of 0.5 mg/mL heparin sodium solution through the tail vein (ie, administered at a dose of 1000 U/kg). Experimental group 1 (low-dose group) was injected with UFH-GNPs with an iron mass of 125 pg via the tail vein of each mouse. Experimental group 2 (high-dose group) was injected with UFH-GNPs with a mass of 250 pg of iron through the tail vein of each mouse. Each mouse in each group was given consecutive tail vein administration for 7 days, and each day was administered at the same time point.

Bleeding time detected by mouse tail docking method: After the last administration on the seventh day, the effect of heparin sodium solution on anticoagulant activity in mice was detected by tail docking method 20 minutes after administration of the positive control group. The two experimental groups also began to detect the effect of UFH-GNPs on the anticoagulant activity of mice 20 minutes after administration. The specific operation of the mouse tail docking method is as follows: Fix the mouse in the holder so that the tail is fully exposed, the tail is vertical, and the mark is made at a distance of 3mm from the tip of the tail. Use surgical scissors to cut off the tip of its tail at the marked place, and start timing when the blood overflows on its own. Use filter paper to absorb larger blood droplets in the middle, until there are no blood stains when the blood droplets are absorbed by filter paper. That is, the bleeding time is recorded (the bleeding time exceeding 1800s is calculated as 1800s).

Conclusion: From the tail bleeding time of mice measured within the specified time after administration, it can be seen that the bleeding time of the negative control group is about 300s, and the bleeding time of the positive control group is about 1800s. There was an extremely significant difference between the negative control group and the positive control group ($P<0.001$), proving the powerful anticoagulant ability of heparin. This result indicates that UFH-GNPs are obtained by modifying GNPs with highly anticoagulant Hep as a surface modifier.

At the two doses observed, there was no significant effect on coagulation in mice (p>0.05).

Bare metal ions and their complexes are known to be toxic to biological systems (23-25), and modification of their surfaces with biocompatible materials can alleviate the toxicity to biological systems and endow them with new properties. Commercially available contrast agents have been surface-modified with natural polymers. In this study, GAGs, which are widely present in organisms, are used as modifiers to explore the feasibility of modifying GNPs for PET/CT contrast agents. This chapter systematically investigates the biocompatibility of GAGs-GNPs.

Tissue Distribution of Contrast Agents in Mice

Grouping: Mice were randomly divided into 4 groups, including the normal control group, UFH-GNPs administration group, LCS-GNPs administration group and LHA-GNPs administration group. Blood and organ samples were collected at six-time points of 0.25h, 0.5h, 1h, 4h, 24h and 48h after administration, and 5 mice were set at each time point in each group.

Dosing scheme: Mice in the normal control group were given 0.2 mL of normal saline via the tail vein.UFH-GNPs administration group, LCS-GNPs administration group and LHA-GNPs administration group mice tail vein injection of iron ion concentration 5mg/kg body weight of the corresponding drug, the volume of the injection liquid is 0. 2mL.

Specimen collection: After the tail vein administration of mice in each group, the mice were anesthetized with ether at six-time points of 0.25h, 0.5h, 1h, 4h, 24h and 48h. The blood of mice was collected in a 1.5mL anticoagulant tube containing EDTA by removing the eyeball and taking blood. After blood samples were collected from each group, the mice were sacrificed by cervical vertebrae, and six tissue samples of heart, liver, spleen, lung, kidney and brain were quickly dissected.

Data processing: Graphpad Prism 5.0 software was used for statistical analysis, and measurement data were expressed as mean ± standard deviation (Dus). One-way ANOVA was used for comparison between groups, and P<0.05 was considered statistically significant. The half-life of each plasma sample was calculated using DAS 2.0 software.

Conclusion: The determination results of plasma iron content in each group at each time point are shown in Figure 8A. As can be seen from Figure 8A, after the administration of GAGs-GNPs through the tail vein, the iron content in the plasma gradually decreased, and the iron content in the plasma was comparable to that of the blank control group at 4 h after administration.

The iron content of UFH-GNPs, LCS-GNPs and LHA-GNPs at different time points in plasma after administration was analyzed by DAS2.0 software. The half-life of each contrast agent in mice can be known (U/2), and the time-dependent curve of iron concentration in plasma after administration of the contrast agent is shown in Figure 8B. The elimination of UFH-GNPs, LCS-GNPs and LHA-SWONs in mice was consistent with the two-compartment model.

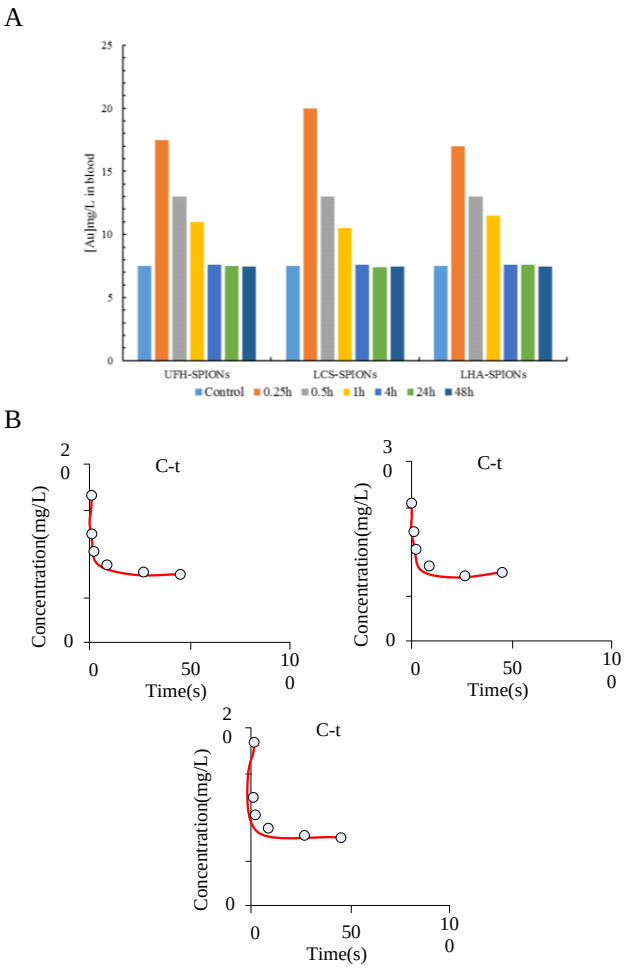

Figure 8. Iron content for analysis. A) Determination of iron content in plasma at each time point of different contrast agents, B) Variation curve of iron ion

concentration in plasma of different contrast agents with time

Imaging Effect of Contrast Agent PETCT

Methods: Nude mice with an obvious tumor in the right forelimb were anesthetized by inhalation of 2.5% isoflurane. During PET/CT, a dose of 0.5-1.5% isoflurane was used to maintain the anesthesia of the mice, and the body temperature of the mice was maintained between 36-37°C and sufficient oxygen supply was ensured for the mice. The respiratory rate and body temperature of the mice were also monitored. The anesthetized mice were fixed in a supine position and placed in the lumen of a PET/CT scanner to collect PET/CT images of the tumor-bearing site before the contrast agent was administered to the mice. Afterward, LCS-GNPs, UFH-GNPs, and LHA-GNPs were injected into tumor-bearing nude mice at a dose of 5 mg/kg body weight through the tail vein based on the iron concentration, and the body position of the nude mice was kept unchanged during the injection process. At 15, 30, 60, 90, and 120 min after administration, the r2-weighted PET/CT images and the corresponding StN information of liver cancer tissue sites in tumor-bearing nude mice were collected. The r2-weighted imaging parameters are set as follows. Fast spin-echo, TR=400.0ms, TE=10.0ms, view=40mmX40mm field and matrix size=128X128, slice thickness=1mm (12 slices, gap=0), 1 average and BW=50kHz. According to the change of the image StN ratio, with the time as the abscissa axis and the image StN ratio change rate as the ordinate axis, the image of the change of the image StN ratio with time after administration was drawn.

Results: PET/CT can obtain 3D anatomical images of soft tissue with high contrast in multiple dimensions. The PET/CT imaging results of LCS-GNPs, UFH-GNPs, and LHA-GNPs in mouse cancer tissue and adjacent tissue after intravenous administration are shown in Figure 9.

As shown in Figure 9, the left area of each image is the paracancerous tissue, and the right side is the cancerous tissue. It can be seen from this result that under the action of an external magnetic field before the contrast agent is administered, PET/CT can clearly distinguish the paracancerous tissue from the cancerous tissue, but the distinction between the local small lesions and the normal tissue in the paracancerous tissue is vague (the black area is larger). After the contrast agent was administered, the cancerous area in the adjacent tissue could not absorb and phagocytose GAGs-GNPs and the corresponding area became brighter. Normal tissue can take in the area corresponding to GAGs-GNPs, and the image becomes darker, which can clearly distinguish the lesion and normal tissue in the adjacent tissue, and improve the development efficiency of PET/CT local lesion imaging. This indicates that intravenous injection of LCS-GNPs, UFH-GNPs, and LHA-GNPs can improve the imaging efficiency of PET/CT and enhance the detection efficiency of focal liver disease. It can also be seen from Figure 9 that the detection rates of small tumor foci in the paracancerous tissue of the PET/CT72-weighted images after intravenous injection of the above three kinds of GAGs-GNPs were improved to varying degrees. The effect of angiography within one hour is more significant, and the detection rate of local lesions is also higher. Among them, the best ability to enhance the imaging effect was achieved before and after 60 minutes; after 60 minutes of contrast agent injection, it still had the ability to enhance the imaging effect, and still had the effect of enhancing the detection rate of lesions.

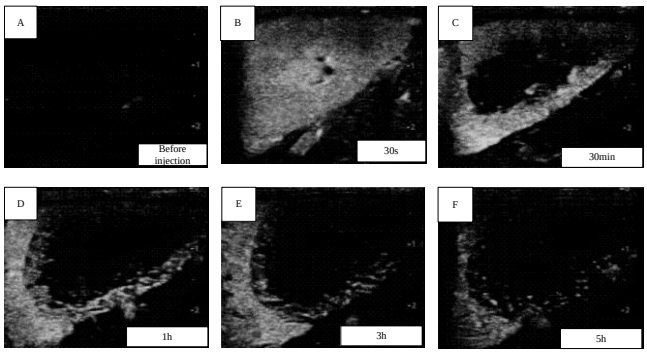

Figure 9. Contrast images at different times after administration

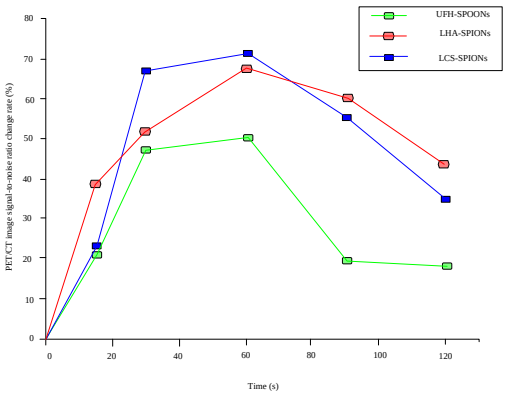

Figure 10. Image SNR change rate

Figure 10 shows the change rate of the StN ratio of the weighted image of the tumor-bearing mouse liver cancer tissue before and after administration. The PET/CT StN ratio is the quotient of the signal value from protons in the patient divided by the sum of the patient noise plus the noise inherent in the electronics. The higher the StN ratio value, the clearer the image presented by the device. The larger the StN ratio change rate, the higher the image quality and the higher the definition.

It can be seen from Figure 10 that after the contrast agent was administered to the liver tumor-bearing model mice, the rate of change of the StN ratio of the PET/CT images showed a trend of first increasing and then decreasing. And at 60 min after contrast agent administration, the change rate of the StN ratio of liver cancer tissue images in LCS-GNPs, UFH-GNPs, and LHA-GNPs groups reached the maximum value, which increased by 50.68%, 67.22%, 71.75% compared with that before contrast agent injection. It can be seen from the results in Figure 10 that the ability of GAGs-SPION to enhance the StN ratio is LHA-GNPs>UFH-GNPs>LCS-GNPs. The decrease in the rate of change of the PET/CT StN ratio after 60 min indicated that LCS-GNPs, UFH-GNPs, and LHA-GNPs were gradually being metabolized in mice.

Conclusions

The ability of UFH-GNPs and LHA-GNPs prepared in this subject to enhance the StN ratio of PET/CT images in the BALB/c nude mouse model of liver cancer is 67.22% and 71.75%, respectively. The ability to improve the contrast efficiency is higher than that of traditional contrast agents. In addition, the contrast agent of UFH-GNPs and LHA-GNPs is higher than that of Auridex, which has been used clinically. In the study of this chapter, it was found that the ability of LCS-GNPs to improve the contrast efficiency was the lowest, only 50.68%. However, the results are similar to the contrast-enhancing capabilities of Auridex, which also shows potential as an r2 contrast agent. The LCS-GNPs, UFH-SHONs, and LHA-GNPs prepared in this subject were administered to mice through the tail vein for 1 h to 2 h, and the rate of change in the StN ratio of PET/CT images began to decrease. The StN ratio change rate of UFH-GNPs was still more than 20% enhanced when the contrast agent was administered for 2 h compared with that before the contrast agent was administered. It shows that GAGs-GNPs have a long residence time in the body, and can be used for multiple imaging at different time points to improve the development efficiency. In conclusion, according to the PET/CT imaging of tumor-bearing nude mice, the LCS-GNPs, UFH-GNPs, and LHA-GNPs developed in this project can significantly improve the contrast efficiency of images, and are very promising contrast agents.

Acknowledgments

Not applicable.

Interest conflict

The authors declare that they have no conflict of interest.

References

1. Karim N, Muhamad NQ, Hamzah F. Primary pulmonary primitive neuroectodermal tumour: potential role of f18-fdg pet/ct as an imaging biomarker. Malays J Med Health Sci 2019; 15(SUPP9):204-206.
2. Sadaghiani M S, Rowe S P, Sheikhbahaei S. Applications of artificial intelligence in oncologic 18F-FDG PET/CT imaging: a systematic review. Ann Transl Med 2021; 9(9):823-823.
3. Saer M S, Bilgi S, Uslu L, Asa S, Snmezolu K. Active Giant Cell Vasculitis Diagnosis with 68Ga PSMA PET/CT Imaging. Mol Imaging Radionucl Ther 2021; 30(1):57-59.
4. Dhull R S, Joshi A, Saha A. Nuclear Imaging in Pediatric Kidney Diseases. Indian Pediatr 2018; 55(7):591-597.
5. Hu C, Wang P, Zhou T, Vallières M, Xu C, Zhu A, et al. FDG-PET/CT Radiomics Models for

The Early Prediction of Locoregional Recurrence in Head and Neck Cancer. Curr Med Imaging 2021; 17(3):374-383.
6. Baek S. A data-driven maximum likelihood classification for nanoparticle agent identification in photon-counting CT. Phys Med Biol 2021; 66(14):145004-145014.
7. Zhao W, Chen L, Wang Z, Lin A, Wang, Zhi M, et al. An albumin-based gold nanocomposites as potential dual mode CT/MRI contrast agent. J Nanopart Res 2018; 20(2):40-56.
8. Kee P H, Danila D. CT imaging of myocardial scar burden with CNA35-conjugated gold nanoparticles. Nanomedicine 2018; 14(6):1941-1947.
9. Shanmugasundaram T, Radhakrishnan M, Gopikrishnan V. In vitro antimicrobial and in vivo wound healing efAuct of actinobacterially synthesised nanoparticles of silver, gold and their alloy. RSC Adv 2017; 7(81):51729-51743.
10. Jian Z, Lakowicz JR. A superior bright NIR luminescent nanoparticle preparation and indicating calcium signaling detection in cells and small animals. Cell and Biosci 2018 8(1):37-43.
11. Tan B, Guo J, Wang L, Chen B. Application value of 18F-FDG PETCT imaging in the clinical initial diagnosis and follow-up of primary lesions of cervical cancer. Transl Cancer Res 2020; 9(6):4005-4010.
12. Cook S, Wilson D, Pourghiasian M. Utility of PETCT over conventional imaging in ovarian cancer. J Clinic Oncol 2018; 36(15_suppl):e17522-e17522.
13. Sorenson E C, Choudhry A J, Yu J Q, Reddy SS, Sigurdson E R. Predictive value of PET/CT for pathological complete response and survival in patients with locally advanced rectal cancer . J Clin Oncol 2017; 35(4_suppl):697-697.
14. Calais J, Czernin J, Aundler WP, Elashoff D, Nickols N G. Randomized prospective phase 3 trial of 68Ga-PSMA-11 PET/CT molecular imaging for prostate cancer salvage radiotherapy planning [PSMA-SRT]. J Clin Oncol 2019; 37(15_suppl):TPS5101-TPS5101.
15. You H, Sanli Y, Subramaniam R M. Impact of Point-Spread Function Reconstruction on 68 Ga-DOTATATE PET/CT Quantitative Imaging Parameters. Am J Roentgenol 2019; 213(3):1-6.
16. Soliman K, Qahtani S A, Alenezi A. Relationship between Patient-Dependent Parameters and Radiation Dose Rates Measured around Patients Undergoing PET/CT Imaging Using ^(18)F-FDG. Int J Med Phys Clin Eng Radiat Oncol 2018, 7(3):403-413.
17. Zhang X, Bian Y, Guo F, Wu D, Hu Y. Comparison on semi-quantitative analysis methods of liver 18F-FDG uptake in PET/CT imaging. Chin J Med Imaging Technol 2018; 34(1):68-72.
18. Williams S, Beauregard J M, Roselt P, Moody K, Fisher R, Drummond E, et al. A randomized trial comparing fluorocholine-PET/CT with conventional imaging in prostate cancer. J Clin Oncol 2019; 37(7_suppl):2-2.
19. Bak N, Elli M. 18Fluorine-fluorodeoxyglucose PET/CT Imaging in Childhood Malignancies. Mol Imaging Radionucl Ther 2021; 30(1):18-27.
20. Verweij N, Wee MT, Jongh JD, Laken CJVD, Zwezerijnen GCJ. OP0189 MACROPHAGE PET/CT imaging of the auet can contribute to early prediction of therapy outcome in rheumatoid arthritis. Ann Rheum Dis 2021; 80(Suppl 1):114.1-114.
21. HF Kennecke, P Raghu, B Lin, GL Funk, A Alseidi. Impact of initial imaging with gallium-68 dotatate PET/CT on diagnosis and management of patients with neuroendocrine tumors (NETs): A sequential case series. J Clin Oncol 2019; 37(4_suppl):379-379.
22. Alzimami K. Development and Optimization of Zirconium-89 Production and Clinical TF-PET/CT Imaging Protocols for Breast Tumor Imaging and Immunotherapy Planning: A Review. J Med Imaging Health Inform 2019; 9(2):215-222.
23. Rafiee E, Kahrizi M. Collaboration of Ni, polyoxometalates and layered double hydroxides: synthesis, characterization, electrochemical and mechanism investigations as nano-catalyst in the Heck coupling reaction. Res Chem Intermed 2018;44(12):7289-309. doi: 10.1007/s11164-018-3557-z.
24. Olfati A, Kahrizi D, Balaky ST, Sharifi R, Tahir MB, Darvishi E. Green synthesis of nanoparticles using Calendula officinalis extract from silver sulfate and their antibacterial effects on Pectobacterium caratovorum. Inorg Chem Commun 2021;125:108439. doi: 10.1016/j.inoche.2020.108439.
25. Cerci J J, Fanti S, Group I. Diagnostic performance of Gallium-68 prostate-specific membrane antigen (PSMA) PET/CT imaging in early-relapsed prostate cancer: Phase 3, prospective, multicenter study (IAEA-PSMA study). J Clin Oncol 2021; 39(15_suppl):5078-5078.